Materials and Design 171 (2019) 107691

Contents lists available at ScienceDirect

Materials and Design

journal homepage: www.elsevier.com/locate/matdes

Exchange bias and two steps magnetization reversal in porous Co/CoO layer

Jesús G. Ovejero [a,*], Vanda Godinho [b], Bertrand Lacroix [b,1], Miguel A. García [c], Antonio Hernando [a,d,e], Asunción Fernández [b,*]

[a] Instituto de Magnetismo Aplicado, 'Salvador Velayos', UCM-CSIC-ADIF, Las Rozas, PO Box 155, Madrid 28230, Spain
[b] Instituto de Ciencia de Materiales de Sevilla CSIC-Univ. Sevilla, Américo Vespucio nr.49, 41092 Sevilla, Spain
[c] Instituto de Cerámica y Vidrio (ICV), CSIC, Kelsen 5, E-28049 Madrid, Spain
[d] IMDEA Nanociencia, Campus Universitario de Cantoblanco, C\Faraday, 9, 28049 Madrid, Spain
[e] Donostia International Physics Center (DIPC), Manuel de Lardizabal Pasealekua, E-20018 Donostia, Spain

HIGHLIGHTS

- Sputtering coatings using partially oxidized Co targets and a He/Ar atmosphere creates porous composites of Co/CoO.
- It is possible to create flexible magnetic layers of Co/CoO nanocomposites depositing over Kapton substrates.
- Porous Co/CoO coatings can generate an exchange bias effect similar to Co/CoO bilayers but in layers thicker than 300 nm.
- Controlling the composition and porosity of Co/CoO coatings it is possible to generate two-steps magnetization loops.

GRAPHICAL ABSTRACT

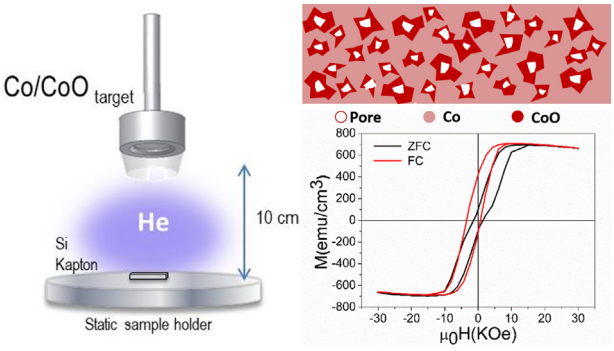

ARTICLE INFO

Article history:
Received 20 November 2018
Received in revised form 4 March 2019
Accepted 5 March 2019
Available online 6 March 2019

Keywords:
Co
Porous
Double loop
Exchange bias

ABSTRACT

In this paper Co/CoO thick layers (hundreds of nanometers) of different porosity and oxidation degree were prepared in a magnetron sputtering deposition process by tailoring the DC sputtering power, as well as the process gas and target composition. The control of the synthesis parameters allowed the nanostructuration of the films with a singular distribution of closed pores and a controlled amount of CoO. We observed an exchange bias field of 2.8 KOe for porous Co/CoO composites, similar to Co/CoO bilayers but for coatings thicker than 300 nm. Besides, it was observed that the coating presents bistable magnetic features when cooled under zero field conditions as a result of the unusual exchange coupling.

1. Introduction

The exchange bias (EB) effect is a magnetic phenomenon that occurs typically in the interface between a ferromagnetic (FM) and an antiferromagnetic material (AFM). Due to the exchange coupling of the two closest layers of spins, the inversion of the magnetization in the FM

* Corresponding authors.
E-mail addresses: jgovejero@ucm.es (J.G. Ovejero), asuncion@icmse.csic.es (A. Fernández).
[1] Current address: Departamento de Ciencia de los Materiales e Ingeniería Metalúrgica y Química Inorgánica, Facultad de Ciencias, Universidad de Cádiz, Spain.

https://doi.org/10.1016/j.matdes.2019.107691

material is hampered for one direction while promoted on the opposite, producing asymmetric hysteresis loops [1]. The shift in the hysteresis loops usually occurs with an enhancement of the coercivity (H_C). In the last decades the EB effect has been applied in magnetic read heads of magnetic information storage devices [2–3], sensors [4–5], spintronic devices [6–7], drug carriers [8] and nanostructured permanent magnets [9].

The EB effect was first discovered by Meiklejohn and Bean [10] in the 50s when studying Co/CoO core-shell nanoparticles cooled below the Néel temperature in the presence of a strong magnetic field. The large exchange coupling between Co and CoO, the convenient Néel temperature of the CoO phase (291 K) [11], and the easy oxidation in a single oxide phase when exposed to air (CoO is formed at room temperature whereas Co_3O_4 requires a heat treatment in the presence of oxygen) [12] make these materials suitable for the study of EB effect [13–14]. Although the first EB studies reported dealt with core-shell nanoparticles [10], thin films have readily attracted the interest of researchers [1,13]. They present a larger FM/AFM interphase area which increases the EB effect and offer a greater number of materials combination.

Nevertheless, the synthesis of thick coatings with effective EB coupling results still challenging [15–16]. Multiple internal surfaces are required to couple the magnetization of the whole FM phase with the bias state of the AFM phase since EB is an interfacial property. Different strategies can be found in literature to promote the coupling between the Co and the CoO phase such as multilayers [17–20], nanocomposite coatings with a random distribution of Co and CoO phases [12,21–23] or films fabricated by assembly of Co/CoO nanoparticles [14,24–25]. In these works the CoO phase is formed either by deposition in the presence of O_2 to generate Co/CoO nanocomposite coatings [21–23] or multilayers [19–20]; by annealing treatments followed by exposure to oxygen [12,17,26] or simply by oxidation in contact with air [25]. The aim of all these approaches is to create a homogeneous distribution of CoO to generate an effective EB coupling with the Co phase.

A rarely explored approach consist on using the nanostructured porosity of the material as a mechanism to control EB coupling. It has been widely reported that the inclusion of antidots (nonmagnetic holes) in magnetic films can modify the magnetic properties of the system [11,27–29]. These dots acts as pinning centers that control the nucleation and propagation of domain walls, inducing a local shape anisotropy that tends to align the magnetization parallel to their edges modifying the coercivity of the coatings [30–32]. On the other hand, the reduction of the lateral dimensions of the FM/AFM structures to dimensions comparable to certain relevant length scales in magnetism (correlation length, domain size, domain wall width etc.) can significantly alter the EB and H_C from those of the continuous films [29,33]. In particular, the relative sizes of the FM and AFM domains determine the overall effect of the EB on a sample [34–35]. Roshchin et al. [34] proposed that if the AFM domains are smaller than the FM ones, the distribution of FM magnetic domains remains recorded in the local orientation of the AFM/FM interfaces when the sample is cooled below its blocking temperature (T_B). Therefore, manipulating the domains size via nanostructuration of the material, it is possible to tune the EB coupling and consequently the magnetic properties of the system.

We have recently demonstrated the possibility to employ our bottom up methodology [36] based on magnetron sputtering deposition using He, to produce cobalt layers with a controlled porous nanostructure [37]. The coating consisted of a polycrystalline cobalt film presenting closed pores (from 4 to 20 nm diameter approximately) homogenously distributed and filled with the deposition gas. This method, presents additional advantages like the possibility to deposit over a wide range of substrates including functional and flexible substrates like polymers [36,38], what results advantageous for the development of flexible electronic devices [39].

In this work we explore the influence of small closed pores –"nanoantidots" – on the magnetic properties of nanocrystalline Co coatings deposited by magnetron sputtering. We show how the CoO formed at room temperature in the target surface when exposed to air, can be used to prepare Co/CoO nanocomposites by magnetron sputtering. The combination of both methodologies was applied to obtain Co/CoO porous nanocomposite thick layers (hundreds of nanometers) exhibiting EB across the whole thickness with magnetic features that can be controlled by the deposition parameters.

2. Experimental section

2.1. Nanostructured Co and Co/CoO films preparation

Co-based layers were deposited on Kapton and silicon (100) substrates, by DC sputtering using a 2″ magnetron from AJA in magnetic target configuration, from a pure cobalt target (Kurt J Lesker, 99.95% pure, 1 mm thick) placed at 10 cm from the sample holder. The base pressure in the chamber before deposition was of $<1 \times 10^{-4}$ Pa. To prepare Co porous coatings, the deposition was carried out using a mixture of He and Ar. Following our previous works [36,40], different deposition power, was used to achieve different pore size. Before deposition, the target was sputter cleaned at 400 W DC in Ar atmosphere (1.0 Pa) in order to eliminate superficial CoO layer or other contaminants (e.g. carbon) formed in contact with air (when opening the deposition chamber).

To prepare the Co/CoO layers we used a pre-oxidized target following the work by Hecq and co-workers [41]. In our case, a previously sputter cleaned target is exposed to a controlled venting procedure and further passivation in air for several hours. The target cleaning conditions (to eliminate possible contaminations different to oxygen) were softer than for Co coatings, in order to maintain the oxide layer. The sputter cleaning was performed at 50 W for 10 min also in Ar atmosphere (1.0 Pa). A dense (non-porous) Co/CoO nanocomposite layer was deposited using Ar atmosphere and a substrate bias voltage of 100 V was set to improve densification of the layer. The porous Co/CoO coating was deposited using a (He + Ar) atmosphere similar to the p-Co layers. Table 1 is an outlook of all the deposition conditions and fabricated samples nomenclature.

2.2. Structural characterization

The structural characterization was carried out on samples deposited over Si substrates. X-ray diffraction measurements were performed using Cu Kα radiation in a Siemens D5000 diffractometer in a Bragg-Brentano configuration in the 2θ angle range of 35–60°. The morphology and thickness of the coatings were studied using scanning electron microscopy (HITACHI S-4800 SEM-FEG). The samples were cleaved from coatings grown onto silicon and observed without metallization in cross-sectional views. To obtain the composition of the films, proton elastic backscattering spectrometry (p-EBS) spectra were obtained at the National Center for Accelerators (CNA, Sevilla, Spain) using a 3MV tandem accelerator. The spectra were measured with a 2 MeV H^+ beam and a surface barrier detector set at 165° as described in reference [42] and simulated using the SIMNRA software [43]. Transmission Electron Microscopy (TEM) analysis were done at the Laboratory of Nanoscopies and Spectroscopies-LANE at the ICMS (Sevilla, Spain) using a FEI Tecnai F30 microscope operated at 300 kV. The microscope works in conventional (TEM), high resolution (HRTEM) and scanning (STEM) operation modes. HRTEM images were submitted to a Fast Fourier Transform (FFT) routine to get digital diffraction patterns. The STEM mode was coupled to a High-Angle Annular Dark Field (HAADF) detector (from Fishione) and an Electron Energy Loss Spectrometer (EELS) from Gatan (GIF Quantum). Cross sectional TEM specimens were prepared in the conventional way by mechanical polishing followed by Ar^+ ion milling to electron transparency of coatings deposited on Si substrates. Before observation, the samples were cleaned inside the TEM holder with and Ar/O_2 plasma. Pores were identified by their bright

Table 1
Sputtering conditions for the growth of Co and Co/CoO coatings.

	Coating	Target cleaning	Power (DC)	Gas mixture	Total pressure	Substrate bias
Co coatings	p_1-Co	400 W	200 W	30%Ar + 70%He	1.2 Pa	–
	p_2-Co	1.0 Pa Ar	400 W	30%Ar + 70%He	1.2 Pa	–
		15 min				
Co/CoO coatings	c-Co/CoO	50 W	50 W	Ar	4.5 Pa	100 V
	p-Co/CoO	1.0 Pa Ar	50 W	30%Ar + 70%He	1.2 Pa	–
		10 min				

contrast in the TEM micrographs. Average pore sizes were determined from binarized micrographs using the "Analyze Particle" function of the ImageJ software [44].

2.3. Magnetic characterization

The magnetic characterization was carried out with samples deposited on Kapton to avoid the strong diamagnetic signal of Si substrates using a SQUID magnetometer (Quantum Design MPMS-5S). Before each measurement, the sample was demagnetized using a decreasing oscillating field from 5 T to 0 T. The magnetization curves were obtained applying a maximum field of 3 T, enough to saturate the sample. Zero Field Cooled (ZFC) and Field Cooled (FC) curves were acquired after cooling the sample without applied field ($H_{FC} = 0$ Oe) and with a maximum applied field ($H_{FC} = 50$ KOe), respectively. In-plane magnetization curves were obtained by fitting the coatings vertically in SQUID capsules and out-of-plane magnetization curves by placing the coatings horizontally in the SQUID capsule between cotton pads. Magnetic volume was estimated using the thickness obtained from SEM cross-sections and the area of the measured sample. The values of coercivity and exchange fields (H_E) were obtained as the half distance and middle point between the fields at which the magnetization curves becomes zero (H_{C1} and H_{C2}), as indicated by Eq. (1).

$$H_C = \frac{H_{C1} - H_{C2}}{2} \quad H_E = \frac{H_{C1} + H_{C2}}{2} \tag{1}$$

3. Results and discussion

3.1. Composition and microstructure of nanostructured Co and Co/CoO coatings

Table 2 presents the thickness obtained from SEM and p-EBS, and the composition of the samples as given by p-EBS. It can be observed that the samples deposited with a sputter cleaning of the Co target at 50 W for 10 min (c-Co/CoO and p-Co/CoO) present a significant degree of oxidation. It confirms that the cleaning conditions were not enough to remove the oxide layer formed at the target surface. Besides, the use of an oxidized target and low DC deposition power results in a lower deposition rate that usually promotes the inclusion of residual oxygen from the chamber [45]. The presence of a small proportion of O in p_1-Co and p_2-Co can be attributed to the incorporation of oxygen from the residual vacuum in the coatings or to a superficial oxidation of the sample during air exposition. The results point out that sputtering with an oxidized target can be used as a strategy to produce partially oxidized coatings with homogeneous composition, at least for layers of hundreds of nanometers in thickness.

The p-EBS results also indicated the presence of He in the samples fabricated with a gas mixture of He and Ar (no signal of Ar was detected). According to our previous works [36–37], it indicates the presence of a certain closed porosity. He is insoluble in almost all metals and tends to form bubbles that remain trapped in the coating after deposition [36,46]. It can be also observed that the increase in sputtering power resulted in higher He content. Besides, the comparison between the thickness values in at/cm^2 given by p-EBS with the thickness measured from SEM cross-sections, indicates that for Co coatings (p_1-Co and p_2-Co) higher sputtering power creates a higher porosity. A small amount of He was incorporated in the composite coating p-Co/CoO but the SEM and p-EBS thicknesses indicated similar porosity to the Co samples.

XRD measurements (Fig. 1) were carried out to evaluate the crystalline structure of the Co and CoO phases. The diffraction patterns of p_1-Co and p_2-Co indicate the formation of the hexagonal h-Co phase with a main (002) peak at 44.5°, highly crystalline in the case of p_1-Co. The absence of (101) reflection indicates a preferential orientation in the deposition of Co crystals. The higher deposition power associated to higher incorporation of He in the p_2-Co coating seems to result in smaller crystal size indicated by a wide (002) peak.

In addition to Co peaks, a strong (111) reflection of cubic CoO phase was detected at 36.5° for c-Co/CoO sample. The absence of the cubic CoO

Table 2
Structural and compositional characterization of the samples synthesized: thickness of deposited layers (Thickness SEM); sputtering deposition rates (Dep rate); atoms per square centimeter from p-EBS measurements (Thickness p-EBS); average percentage of Co, He and O from p-EBS measurements (Composition p-EBS). *Calculated from SEM cross-sections micrographs.

Coating	Thickness SEM* (nm)	Dep rate* (nm/min)	Thickness p-EBS (10^{15} at/cm^2)	Composition p-EBS		
				Co (at%)	He (at%)	O (at%)
p_1-Co	1500	25	14 500	87	5	8
p_2-Co	460	30.6	2900	80	14	6
c-Co/CoO	100	1.5	1025	61	–	39
p-Co/CoO	350	2.9	3000	63	3	34

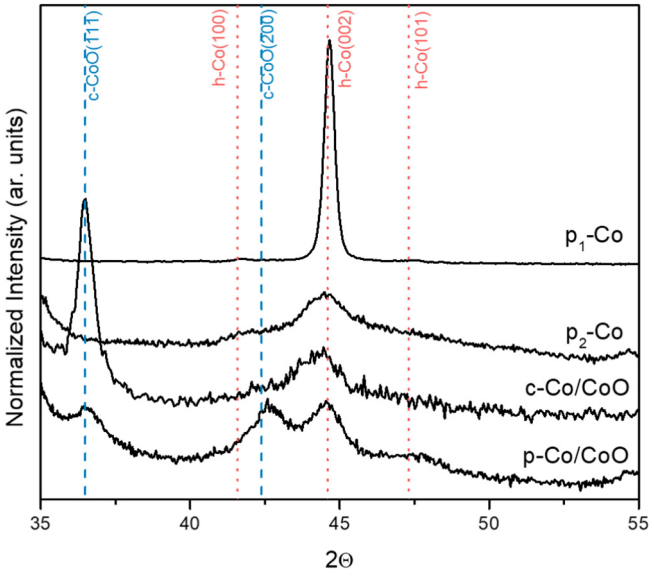

Fig. 1. XRD measurements of the prepared coatings. The position of the hexagonal Co (red) and cubic CoO (blue) phases are indicated with vertical dash lines.

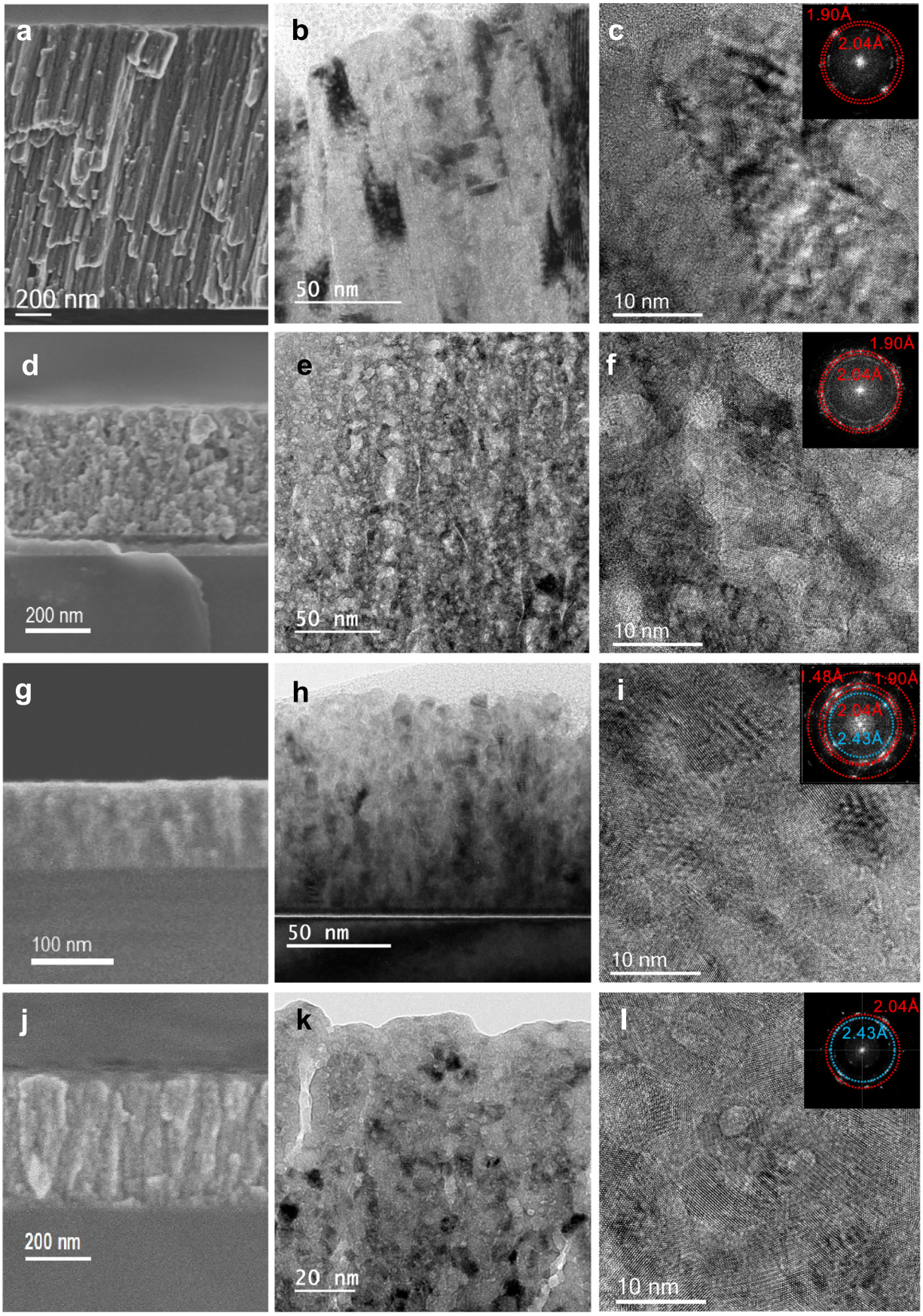

Fig. 2. SEM (left), TEM (middle) and HRTEM (right) cross-sectional micrographs of samples: p_1-Co (a-c), p_2-Co (d-f), c-Co/CoO (g-i) and p-Co/CoO (j-l). The corresponding FFT of HRTEM images are displayed in the insets, indicating the main reflections correspond to interplanar distances of the hexagonal cobalt (red circles) and cubic CoO (blue circle) phases.

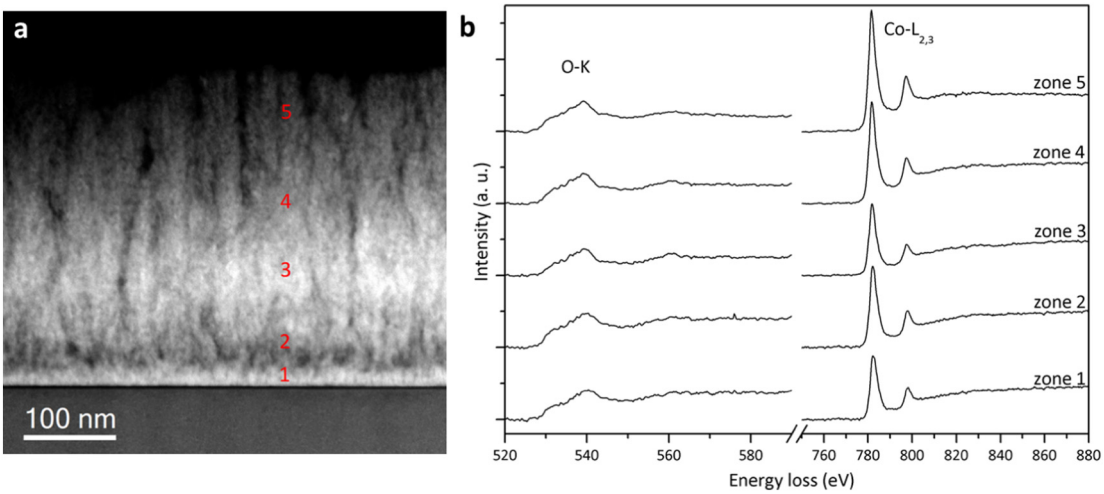

Fig. 3. a) STEM-HAADF image of sample p-Co/CoO, b) EELS analysis of the marked zones in a) showing O-K and Co-L2,3 edges (extracted from the background by power-law fitting).

(200) reflection suggests a preferential orientation of the oxide phase in this sample grown under substrate bias. The p-Co/CoO sample, prepared with He and without substrate bias, presents a wider CoO peaks and consequently a smaller crystal size. These results prove that the samples prepared at soft sputter cleaning conditions are indeed composite coatings of Co and CoO with well defined crystalline phases.

Figs. 2, present the morphology and microstructure of the samples by SEM (left) and TEM (middle) and HRTEM (rigth). Fig. 2a and b show the columnar morphology and the porosity of the p_1-Co coating. The high-resolution image presented in Fig. 2c shows that the columns contain very small pores (areas with lighter contrast) with an approximate average size of 1.5 nm. The fast Fourier transform (FFT) analysis indicates the presence of large crystals of the hexagonal phase of Co, in agreement with XRD measurements.

A porous structure with bigger pores was observed for the p_2-Co sample in the SEM micrograph of Fig. 2d. In this sample, prepared at higher sputtering power, the TEM cross-sections (Fig. 2e and f) show a structure of small pores (average size ~5 nm) and also interconnected pores forming bigger channels. In the HRTEM micrograph of Fig. 2f the crystalline planes of the hexagonal Co phase around the pores can be seen in more detail. The FFT of Fig. 2f is also in agreement with the presence of hexagonal Co nanocrystals.

c-Co/CoO coating (Fig. 2g-i) presents a more compact structure in SEM cross section, as expected for substrate biased coatings. The HRTEM study reveals that the nanocomposite structure is composed by a mixture of hexagonal Co and cubic CoO crystals homogenously distributed.

In the case of p-Co/CoO coating (prepared with He), the SEM cross-section in Fig. 2j reveals a porous columnar like structure, presenting also small round pores. These pores can be observed in more detail in Fig. 2k and l. In this case the sample presents isolated pores of approximate average size of 5 nm, and some interconnected pores forming channels. The HRTEM image shows the pores in detail and the FFT confirms the presence of Co and CoO crystals.

STEM-HAADF/EELS analysis of the coatings was performed to study the homogeneity of the CoO phase distribution in p-Co/CoO. Fig. 3 presents O-K and Co-$L_{2,3}$ edges of sample p-Co/CoO measured in different zones across the coating thickness. The results show a similar proportion of cobalt oxide across the sample thickness [47]. The presence of He was studied by analyzing the low energy loss region of EELS spectra in p_2-Co and p-Co/CoO samples (Figs. S1 and S2 of Supporting information). A He-K edge signal was detected for the spectra acquired inside the pores but not in those acquired in the matrix. In both samples a small peak corresponding to the He-K edge at around 22–25 eV

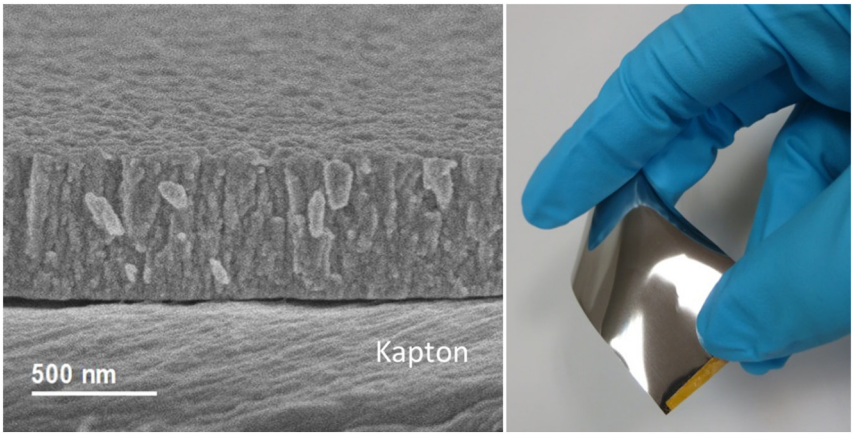

Fig. 4. a) SEM cross-sectional micrograph of a sample prepared under similar conditions to p-Co/CoO over Kapton, b) photograph showing the coating on Kapton.

(depending on the pore size) was observed across the pores, indicating that pores are filled with a He density between 10 and 80 He/nm^3, according to Ref. [40].

SEM cross-section in Fig. 4a, shows the morphology of the samples deposited on Kapton substrates which resulted similar to the samples deposited on silicon. The photograph in Fig. 4b reflects the large size and flexibility of the coating deposited on Kapton, worth mentioning that the coating remained well adhered during sample manipulation.

3.2. Magnetic characterization

The magnetic response of each sample was studied through the out-of-plane magnetization curves presented in Fig. 5. Due to the strong shape anisotropy of the films, the most interesting magnetic features of the samples could not been observed in the in-plane magnetization curves (Fig. S3 in SI). Fig. 5a displays the magnetization curve of p_1-Co sample. The cycle presents a soft magnetization inversion with low coercivity ($H_C = 580$ Oe) and remanence ($M_R = 160$ emu/cm^3). This is the usual response in pure metallic Co films for out-of-plane curves. The curve obtained for p_2-Co in Fig. 5b presents similar shape and remanence ($M_R = 220$ emu/cm^3) but smaller coercivity ($H_C = 184$ Oe). As it was indicated in the introduction, the presence of pores in FM materials makes the magnetization bends around the pores to avoid the generation of internal magnetic poles [30]. The rippling of magnetization favors the nucleation of domain walls promoting the inversion of magnetizations and can be the responsible of the smaller coercivity of the sample [28]. Besides, the smaller crystal size observed for p_2-Co (broader XRD peaks in Fig. 1) reduces the anisotropy energy in the grains favoring the magnetic softening of the material. In both samples, the field cooled (FC) and zero field cooled (ZFC) curves were similar.

On the contrary, the loops of c-Co/CoO composite coating in Fig. 5c, show important differences between the symmetric ZFC loop and the shifted FC loop and an enhancement of coercivity up to $H_C = 6.0$ KOe. The EB field ($H_E = 1.5$ KOe) associated to the shifting of the loop is lower than those reported for Co/CoO bilayers in the literature [2,48]. Such small EB effect suggests a poor FM/AFM magnetic coupling likely caused by an inhomogeneous distribution of CoO phase in the coating.

Fig. 5d presents the unusual magnetic response observed in p-Co/CoO layer. Two-steps magnetization reversal appeared in the ZFC curve when the sample was cooled in a demagnetized configuration. When the sample was measured in FC conditions, a shifted loop with a single magnetization reversal was observed instead. The coercivity of FC curve ($H_C = 4.1$ KOe) resulted to be lower than c-Co/CoO layers while the EB field ($H_E = 2.8$ KOe) was almost the double. In this case, the values result similar to those reported for Co-CoO bilayers [2,48].

In order to understand the origin of the two-steps magnetization reversal observed in p-Co/CoO, the sample was characterized at different temperatures and different cooling fields (H_{FC}). Fig. 6a displays the ZFC curves measured at increasing temperatures from 5 K to 300 K. Two-steps magnetization reversals were observed up to 175 ± 15 K (see detailed graph in SI Fig. S5). Above this temperature the magnetization reversal took place in a single step and no shifting of the loop was registered. In Fig. 6b, the FC curves of the sample cooled under strong fields ($H_{FC} = 50$ KOe) show a single-step reversion along the whole range of temperatures. The EB shifting of the curves observed at low temperatures disappears also at 175 ± 15 K. The discrepancy between the blocking temperature (temperature at which exchange bias disappears, T_B) and the Neel temperature (T_N) of CoO have been widely reported for exchange bias systems [12,48–49]. It is commonly explained in terms of the interfacial anisotropy energy generated by the roughness in the interface of FM and AFM phases [50].

In Fig. 6c, it can be observed that the H_{FC} transition between single-step and two-steps magnetization reversal at 5 K takes place at 5 KOe, which is close to saturation field observed at 300 K ZFC cycles (see Fig. 5d). If the H_{FC} is bellow this threshold but different to zero (1 KOe), the reversal of the magnetization takes place in two-step, despite a preferential direction is defined and the vertical symmetry of the curve is broken.

Fig. 6d quantifies the dependence with the temperature of the H_C and H_E in the curves obtained at the different H_{FC}. It is possible to observe that H_E drops with the temperature in every $H_{FC} > 0$ and becomes zero at T_B. Besides, H_C is also higher when the sample is cooled at high H_{FC}. Coercive value is doubled for cooling fields equal or higher than 5 KOe respect to ZFC curve but does not present big differences between one another. The differences in H_C for high and low H_{FC} disappear close to T_B as well, and all the curves collapse into a single common trend above this temperature.

The collapse of H_E and H_C curves at the same temperature as well as the vanishing of the two steps magnetization reversal in ZFC curves, suggest that we are observing an EB effect for all the cases. Accepting this, ZFC curve at 5 K (Fig. 6a) can be explained considering that when a demagnetized sample is cooled down, the FM domain structure presents the same number of domains pointing in opposite directions. In this way, during the cooling process the FM domains fix a half of the AFM surface spins on one direction and another half on the opposite. Consequently, at low temperature each half of the FM domains will suffer opposite EB effect, splitting the loop in two sub-loops, as observed in Fig. 6a. In other words, the demagnetized domain structure of the FM remains recorded in the AFM surfaces when crossing the T_B of the system. Such explanation is confirmed by two characteristic features of the curves. First, the shifting observed for each part of the curve is symmetric in the case of $H_{FC} = 0$ (i.e. completely demagnetized sample). Second, for that case the magnetization decreases to its half in each inversion.

The vertical symmetry is broken when the sample is slightly magnetized ($H_{FC} = 1$ KOe). As a consequence of the field applied during the cooling, the number of domains pointing in each direction is not well-balanced and a preferential EB direction is created. Two-steps magnetization reversal definitively disappears when the sample is saturated and all the AFM surfaces are fixed in the same direction producing a coherent EB effect. Such dependence with the H_{FC} confirms that the two-steps magnetization reversal is not a consequence of the uncoupled magnetic phases but a genuine EB effect [51].

Analogue double-inverse processes have been observed in bilayers, multilayers and even some alloys [12,52–54], but it had not been reported before in porous materials. Dobrynin et al. [25] explained a similar effect observed in layers of oxidized Co clusters as a coexistence of exchange bias and exchange spring effect. However, such studies assumed a continuous CoO matrix with Co crystals embedded, not taking into account the porosity of the sample (nonmagnetic inclusions) [25,55]. As mentioned in the introduction, Roshchin et al. [34] postulated the ratio between AFM and FM domain sizes as a key parameter for the observation of the double magnetization curves in exchange coupled systems [34]. This effect requires AFM domains sizes to be smaller than the FM domains in order to fix the FM domain configuration in the AFM memory.

The two step cycles observed in p-Co/CoO and the enhancement in H_{EB} respect to c-Co/CoO sample indicate that the porosity plays a significant role in the homogeneous distribution of CoO phase in the sample. These phenomena can be explained assuming that CoO preferentially occupies the regions around the pores and considering the average pore size observed in TEM images of p-Co/CoO. Using the ratio between SEM and p-EBS thicknesses and the magnetization of the sample, it was estimated that the CoO phase could form hollow AFM domains of 8 nm around the pores (see details in SI). On the other hand, the typical critical diameter for single domain in hcc Co crystal is 162 nm [56].

These numbers indicate that under this hypothesis multiple AFM shells can be fitted in a single FM domain of Co, satisfying the Roshchin criteria for double-shifted magnetization curves. On the other hand, the magnetic correlation length in Co (51 nm) [56] results larger than the inter-pore distance, thus the whole Co matrix can be coupled with the CoO formed around the pores. As a consequence of that any sign of

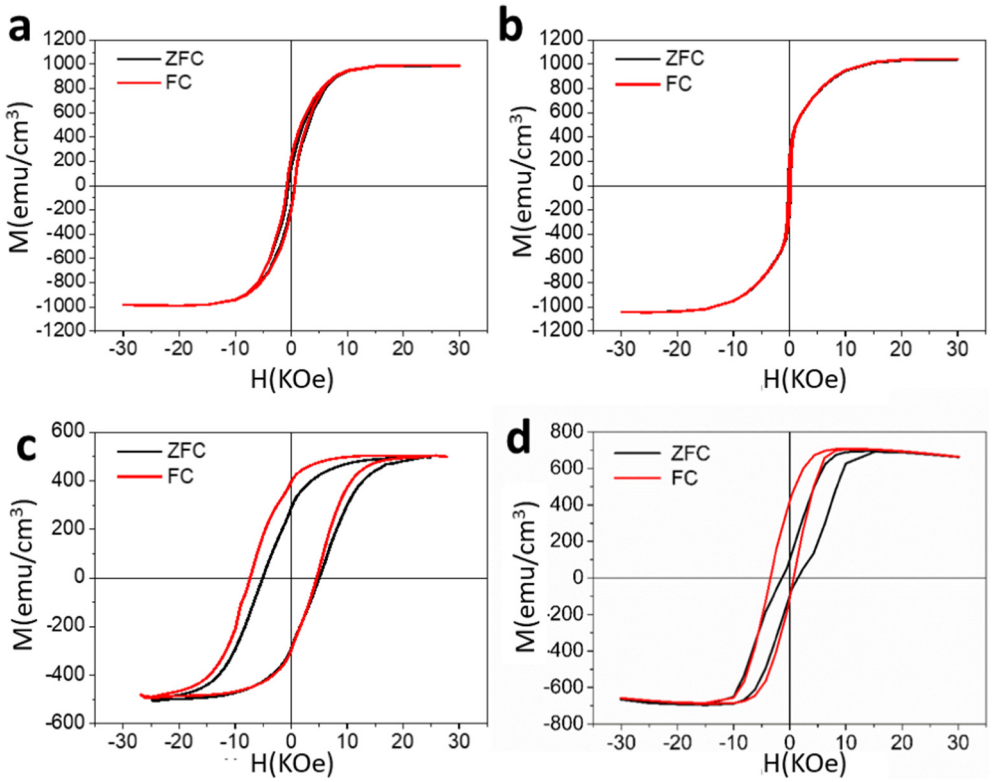

Fig. 5. Out of plane magnetic curves measured at 5 K when cooling the samples in zero field cooled (black line) and field cooled (red line) conditions: a) p1-Co, b) p2-Co, c) c-Co/CoO and d) p-Co/CoO.

exchange coupling independent inversion in FC curves was observed and the EB effect resulted comparable to the one observed in Co/CoO bilayers [2,48]. Therefore, the introduction of porosity by magnetron sputtering of Co-CoO layers using He as deposition gas, is presented in this work as a novel strategy to produce magnetic layers of hundreds of nanometers with tunable EB effect and a H_{EB} similar to that observed in thin bilayers.

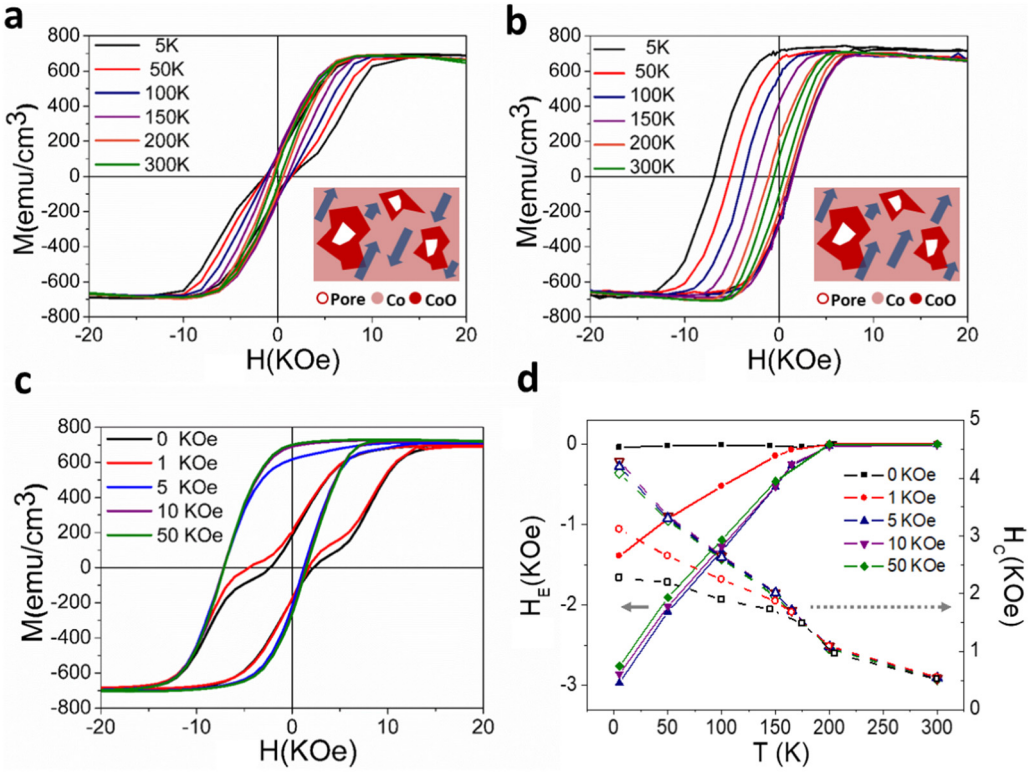

Fig. 6. Magnetization curves of p-Co/CoO sample measured at increasing temperatures in: a) zero field cooled conditions; b) field cooled conditions ($H_{FC} = 50$ KOe). Magnetization curves at 5K for increasing cooling fields. d) Evolution of exchange bias field (H_E, filled symbols) and coercive field (H_C, empty symbols) with temperature for samples cooled with different cooling fields. The insets show plausible remanent states of the FM phase in (a) zero field cooled and (b) field cooled conditions.

4. Conclusions

Co and Co/CoO sputtered layers can be deposited by controlling the target cleaning process. Different porosity can be also achieved by selection of the deposition working gas (Ar and/or He). The nanostructuration of the coating by the introduction of pores (nonmagnetic holes) and the formation (or not) of the Co/CoO nanocomposite have been related to the magnetic behavior of the different samples. It has been observed that the amount of CoO phase and the porosity can be employed to produce a field-tunable exchange bias effect comparable to Co/CoO bilayers for coatings of hundreds of nanometers.

CRediT authorship contribution statement

Jesús G. Ovejero: Data curation, Formal analysis, Writing - original draft. **Vanda Godinho:** Data curation, Formal analysis, Writing - original draft. **Bertrand Lacroix:** Data curation, Formal analysis, Writing - review & editing. **Miguel A. García:** Funding acquisition, Formal analysis, Writing - review & editing. **Antonio Hernando:** Formal analysis, Funding acquisition, Writing - review & editing. **Asunción Fernández:** Formal analysis, Funding acquisition, Writing - review & editing.

Acknowledgments

In memoriam Dr. Patricia Crespo del Arco. This work has been supported by the Spanish Ministry of Science and Innovation (projects MAT2012-37109-C02 and 01; MAT2017-86540-C4-1-R; CTQ2015-65918-R, EU co-financed by FEDER); the CSIC (PIE 201760E002) and H2020-LEIT-NMBP/0248; Regional Government of Madrid through Projects S2013/MIT-2850(NANOFRONTMAG) and P2018/NMT-4321 (NANOMAGCOST). The authors also acknowledge the Laboratory for Nanoscopies and Spectroscopies for the TEM facilities and the technical assistance of I. Rosa, O. Montes and M.R. García.

Appendix A. Supplementary data

See supplementary material for the complete structural and magnetic characterization of the porous Co/CoO layers. Supplementary data to this article can be found online at https://doi.org/10.1016/j.matdes.2019.107691.

References

[1] J. Nogues, I.K. Schuller, Exchange bias, J. Magn. Magn. Mater. 192 (2) (1999) 203–232.
[2] J. Nogues, J. Sort, V. Langlais, V. Skumryev, S. Surinach, J.S. Munoz, M.D. Baro, Exchange bias in nanostructures, Phys. Rep. 422 (3) (2005) 65–117.
[3] S. Parkin, X. Jiang, C. Kaiser, A. Panchula, K. Roche, M. Samant, Magnetically engineered spintronic sensors and memory, Proc. IEEE 91 (5) (2003) 661–680.
[4] D.C. Leitao, A.V. Silva, E. Paz, R. Ferreira, S. Cardoso, P.P. Freitas, Magnetoresistive nanosensors: controlling magnetism at the nanoscale, Nanotechnology 27 (4) (2016).
[5] P.P. Sharma, E. Albisetti, M. Monticelli, R. Bertacco, D. Petti, Exchange bias tuning for magnetoresistive sensors by inclusion of non-magnetic impurities, Sensors 16 (7) (2016).
[6] E. Albisetti, A. Calò, M. Spieser, A.W. Knoll, E. Riedo, D. Petti, Appl. Phys. Lett. 113 (2018), 162401.
[7] E. Albisetti, D. Petti, Domain wall engineering through exchange bias, J. Magn. Magn. Mater. 400 (2016) 230–235.
[8] B. Issa, I.M. Obaidat, B.A. Albiss, Y. Haik, Magnetic nanoparticles: surface effects and properties related to biomedicine applications, Int. J. Mol. Sci. 14 (11) (2013) 21266–21305.
[9] E. Lottini, A. Lopez-Ortega, G. Bertoni, S. Turner, M. Meledina, G. Van Tendeloo, C.D. Fernandez, C. Sangregorio, Strongly exchange coupled core|shell nanoparticles with high magnetic anisotropy: a strategy toward rare-earth-free permanent magnets, Chem. Mater. 28 (12) (2016) 4214–4222.
[10] W.H. Meiklejohn, C.P. Bean, New magnetic anisotropy, Phys. Rev. 102 (5) (1956) 1413–1414.
[11] A. Sharma, J. Tripathi, K.C. Ugochukwu, S. Tripathi, Optimization of exchange bias in Co/CoO magnetic nanocaps by tuning deposition parameters, Solid State Commun. 254 (2017) 1–5.
[12] L. Lukashuk, K. Föttinger, E. Kolar, C. Rameshan, D. Teschner, M. Hävecker, A. Knop-Gericke, N. Yigit, H. Li, E. McDermott, M. Stöger-Pollach, G. Rupprechter, J. Catal. 344 (2016) 1–15.
[13] H.-L. Liu, S. Brems, Y.-J. Zeng, K. Temst, A. Vantomme, C. Van Haesendonck, J. Phys. Condens. Matter 28 (2016), 196002.
[14] J.A. González, J.P. Andrés, R. López Antón, J.A. De Toro, P.S. Normile, P. Muñiz, J.M. Riveiro, J. Nogués, Maximizing exchange bias in Co/CoO core/shell nanoparticles by lattice matching between the shell and the embedding matrix, Chem. Mater. 29 (12) (2017) 5200–5206.
[15] R. Morales, A.C. Basaran, J.E. Villegas, D. Navas, N. Soriano, B. Mora, C. Redondo, X. Batlle, I.K. Schuller, Exchange-bias phenomenon: the role of the ferromagnetic spin structure, Phys. Rev. Lett. 114 (9) (2015), 097202.
[16] M. Kiwi, Exchange bias theory, J. Magn. Magn. Mater. 234 (3) (2001) 584–595.
[17] L. Hao-Liang, B. Steven, Z. Yu-Jia, T. Kristiaan, V. André, H. Chris Van, Interplay between magnetocrystalline anisotropy and exchange bias in epitaxial CoO/Co films, J. Phys. Condens. Matter 28 (19) (2016), 196002.
[18] D. Kumar, S. Singh, A. Gupta, Effect of interface roughness on exchange coupling in polycrystalline Co/CoO bilayer structure: an in-situ investigation, J. Appl. Phys. 120 (8) (2016), 085307.
[19] M. Öztürk, E. Sınır, E. Demirci, M. Erkovan, O. Öztürk, N. Akdoğan, Exchange bias properties of [Co/CoO]n multilayers, J. Appl. Phys. 112 (9) (2012), 093911.
[20] J. Wang, T. Sannomiya, J. Shi, Y. Nakamura, Influence of interface roughness on the exchange bias of Co/CoO multilayers, J. Appl. Phys. 113 (17) (2013) 17D707.
[21] M. Ohkoshi, K. Tamari, S. Honda, T. Kusuda, Microstructure and exchange anisotropy of Co-CoO films with perpendicular magnetization, J. Appl. Phys. 57 (8) (1985) 4034–4036.
[22] J.A. De Toro, J.P. Andrés, J.A. González, P. Muñiz, T. Muñoz, P.S. Normile, J.M. Riveiro, Exchange bias and nanoparticle magnetic stability in Co-CoO composites, Phys. Rev. B 73 (9) (2006), 094449.
[23] J.B. Yi, J. Ding, B.H. Liu, Z.L. Dong, T. White, Y. Liu, Exchange bias and magnetization process of Co/CoO nanocomposite thin films, J. Magn. Magn. Mater. 285 (1) (2005) 224–232.
[24] R. Antón, J. González, J. Andrés, P. Normile, J. Canales-Vázquez, P. Muñiz, J. Riveiro, J. De Toro, Exchange bias optimization by controlled oxidation of cobalt nanoparticle films prepared by sputter gas aggregation, Nanomaterials 7 (3) (2017) 61.
[25] A.N. Dobrynin, D.N. Ievlev, C. Hendrich, K. Temst, P. Lievens, U. Hörmann, J. Verbeeck, G. Van Tendeloo, A. Vantomme, Influence of finite size effects on exchange anisotropy in oxidized Co nanocluster assembled films, Phys. Rev. B 73 (24) (2006), 245416.
[26] R.L. Antón, J.A. González, J.P. Andrés, J. Canales-Vázquez, J.A.D. Toro, J.M. Riveiro, High-vacuum annealing reduction of Co/CoO nanoparticles, Nanotechnology 25 (10) (2014), 105702.
[27] X. Li, C.W. Leung, C.C. Chiu, K.W. Lin, M. Chan, Y. Zhou, P.W.T. Pong, Exchange bias study of sub-100 nm-diameter CoFeB/IrMn antidot and nanodot arrays fabricated by nanosphere lithography, Phys. Lett. A 381 (33) (2017) 2709–2714.
[28] M. Perzanowski, M. Krupinski, A. Zarzycki, A. Dziedzic, Y. Zabila, M. Marszalek, Exchange bias in the [CoO/Co/Pd]10 antidot large area arrays, ACS Appl. Mater. Interfaces 9 (38) (2017) 33250–33256.
[29] D. Tripathy, A.O. Adeyeye, Probing the exchange bias in Co/CoO nanoscale antidot arrays using anisotropic magnetoresistance, Phys. Rev. B 79 (6) (2009), 064413.
[30] L.A. Rodríguez, C. Magén, E. Snoeck, C. Gatel, C. Castán-Guerrero, J. Sesé, L.M. García, J. Herrero-Albillos, J. Bartolomé, F. Bartolomé, M.R. Ibarra, High-resolution imaging of remanent state and magnetization reversal of superdomain structures in high-density cobalt antidot arrays, Nanotechnology 25 (38) (2014), 385703.
[31] S. Michea, J.L. Palma, R. Lavín, J. Briones, J. Escrig, J.C. Denardin, R.L. Rodríguez-Suárez, Tailoring the magnetic properties of cobalt antidot arrays by varying the pore size and degree of disorder, J. Phys. D. Appl. Phys. 47 (33) (2014), 335001.
[32] K. Andreas, P.d.R. Rafael, A. Raquel, P. Juan Luis, A. José, N. Dimitrios, V. Manuel, E. Juan, G.-M. José Miguel, Magnetic properties engineering of nanopatterned cobalt antidot arrays, J. Phys. D. Appl. Phys. 49 (17) (2016), 175004.
[33] F. Spizzo, M. Tamisari, F. Chinni, E. Bonfiglioli, A. Gerardino, G. Barucca, D. Bisero, S. Fin, L. Del Bianco, J. Magn. Magn. Mater. 400 (2016) 242–247.
[34] I.V. Roshchin, O. Petracic, R. Morales, Z.P. Li, X. Batlle, I.K. Schuller, Lateral length scales in exchange bias, EPL 71 (2) (2005) 297.
[35] S. Brück, J. Sort, V. Baltz, S. Suriñach, J.S. Muñoz, B. Dieny, M.D. Baró, J. Nogués, Exploiting length scales of exchange-bias systems to fully tailor double-shifted hysteresis loops, Adv. Mater. 17 (24) (2005) 2978–2983.
[36] V. Godinho, J. Caballero-Hernández, D. Jamon, T.C. Rojas, R. Schierholz, J. García-López, F.J. Ferrer, A. Fernández, A new bottom-up methodology to produce silicon layers with a closed porosity nanostructure and reduced refractive index, Nanotechnology 24 (27) (2013), 275604.
[37] B. Lacroix, V. Godinho, A. Fernández, The nanostructure of porous cobalt coatings deposited by magnetron sputtering in helium atmosphere, Micron 108 (2018) 49–54.
[38] J. Caballero-Hernandez, V. Godinho, B. Lacroix, M.C. Jimenez de Haro, D. Jamon, A. Fernandez, Fabrication of optical multilayer devices from porous silicon coatings with closed porosity by magnetron sputtering, ACS Appl. Mater. Interfaces 7 (25) (2015) 13889–13897.
[39] S. Ping, W. Baomin, L. Runwei, Flexible magnetic thin films and devices, J. Semicond. 39 (1) (2018), 011006.
[40] R. Schierholz, B. Lacroix, V. Godinho, J. Caballero-Hernandez, M. Duchamp, A. Fernandez, STEM-EELS analysis reveals stable high-density He in nanopores of amorphous silicon coatings deposited by magnetron sputtering, Nanotechnology 26 (7) (2015).
[41] M. Hecq, A. Hecq, J. Van Cakenberghe, Étude expérimentale de la pulvérisation cathodique réactive du cobalt, Thin Solid Films 42 (1) (1977) 97–105.

[42] F.J. Ferrer, M. Alcaire, J. Caballero-Hernandez, F.J. Garcia-Garcia, J. Gil-Rostra, A. Terriza, V. Godinho, J. Garcia-Lopez, A. Barranco, A. Fernandez-Camacho, Simultaneous quantification of light elements in thin films deposited on Si substrates using proton EBS (Elastic Backscattering Spectroscopy), Nucl. Instrum. Methods Phys. Res., Sect. B 332 (2014) 449–453.
[43] W. Eckstein, R. Dohmen, H. Friedrich, F. Hertweck, Dependence of energy distributions of sputtered and reflected atoms on incident fluence, Nucl. Instrum. Methods Phys. Res., Sect. B 153 (1–4) (1999) 345–349.
[44] W.S. Rasband, ImageJ, U.S. National Institutes of Health, 543 Bethesda, MD, 2012 , Online: imagej.nih.gov/ij/.
[45] K. Koski, J. Hölsä, P. Juliet, Deposition of aluminium oxide thin films by reactive magnetron sputtering, Surf. Coat. Technol. 116–119 (1999) 716–720.
[46] J.H. Evans, Mechanisms of void coarsening in helium implanted silicon, Nucl. Instrum. Methods Phys. Res., Sect. B 196 (1–2) (2002) 125–134.
[47] Z. Zhang, Surface effects in the energy loss near edge structure of different cobalt oxides, Ultramicroscopy 107 (8) (2007) 598–603.
[48] F. Radu, H. Zabel, Exchange bias effect of ferro-/antiferromagnetic heterostructures, in: H. Zabel, S.D. Bader (Eds.),Magnetic Heterostructures 2008, pp. 97–184.
[49] P.J. van der Zaag, Y. Ijiri, J.A. Borchers, L.F. Feiner, R.M. Wolf, J.M. Gaines, R.W. Erwin, M.A. Verheijen, Difference between blocking and Néel temperatures in the exchange biased Fe_3O_4/CoO system, Phys. Rev. Lett. 84 (26) (2000) 6102–6105.
[50] A.N. Dobrynin, R. Prozorov, Characteristic temperatures of exchange biased systems, J. Appl. Phys. 102 (4) (2007).
[51] A.E. Berkowitz, K. Takano, Exchange anisotropy — a review, J. Magn. Magn. Mater. 200 (1) (1999) 552–570.
[52] I. Betancourt, H.A. Davies, Exchange coupled nanocomposite hard magnetic alloys, Mater. Sci. Technol. 26 (1) (2010) 5–19.
[53] R.L. Wang, M.K. Lee, L.S. Xu, Z.G. Sun, V.V. Marchenkov, C. Tien, J.C.A. Huang, C.P. Yang, Effect of thermal cycle on the interfacial antiferromagnetic spin configuration and exchange bias in Ni-Mn-Sb alloy, AIP Adv. 2 (3) (2012), 032181.
[54] S. Chen, H. Zhao, G. Wang, Z. Zhang, B. Ma, Q.Y. Jin, Double-shifted magnetic hysteresis loops in perpendicular [Co/Ni]N/FeMn exchange biased systems, Thin Solid Films 534 (2013) 553–556.
[55] A.N. Dobrynin, M.J.V. Bael, K. Temst, P. Lievens, Evidence for coexistence of exchange bias and exchange spring effects in oxidized Co nanocluster assembled films, New J. Phys. 9 (8) (2007) 258.
[56] B.D. Cullity, C.D. Graham, Introduction to Magnetic Materials, 2nd edition Wiley-IEEE Press, 2008.